LAWRENCE
LIVERMORE
NATIONAL
LABORATORY

LLNL-JRNL-599778

DIII-D Research toward resolving key issues for ITER and steady-state tokamaks

D. N. Hill

November 8, 2012

Nuclear Fusion

Disclaimer

This document was prepared as an account of work sponsored by an agency of the United States government. Neither the United States government nor Lawrence Livermore National Security, LLC, nor any of their employees makes any warranty, expressed or implied, or assumes any legal liability or responsibility for the accuracy, completeness, or usefulness of any information, apparatus, product, or process disclosed, or represents that its use would not infringe privately owned rights. Reference herein to any specific commercial product, process, or service by trade name, trademark, manufacturer, or otherwise does not necessarily constitute or imply its endorsement, recommendation, or favoring by the United States government or Lawrence Livermore National Security, LLC. The views and opinions of authors expressed herein do not necessarily state or reflect those of the United States government or Lawrence Livermore National Security, LLC, and shall not be used for advertising or product endorsement purposes.

DIII-D Research toward resolving key issues for ITER and steady-state tokamaks

D.N. Hill[a)] for the DIII-D Team

[a)]*Lawrence Livermore National Laboratory, Livermore, CA 94551*

e-mail: hilldn@fusion.gat.com

Abstract. The DIII-D research program is addressing key ITER challenges and developing the physics basis for future steady-state tokamaks. Pellet pacing edge localized mode (ELM) control in the ITER configuration shows energy loss $\propto 1/f_{\mathrm{pellet}}$ at frequencies up to 12x the natural rate, and complete ELM suppression with resonant magnetic perturbations (RMP) is now obtained at the q_{95} expected for ITER baseline scenario discharges. Long-duration ELM-free QH-mode discharges have been produced with ITER-relevant co-current neutral beam injection (NBI) using external $n = 3$ coils to generate sufficient counter-I_{p} torque. ITER baseline discharges at $\beta_{\mathrm{N}} = 2$ and scaled NBI torque have been maintained in stationary conditions for more than four resistive times using electron cyclotron current drive (ECCD) for tearing mode suppression and disruption avoidance; active tracking with steerable launchers and feedback control catch modes early and reduce the ECCD power requirements. Disruption experiments with massive gas injection reveal runaway electron dissipation rates ~10x faster than expected and demonstrate the possibility of benign dissipation in ITER. Other ITER-related experiments show measured intrinsic plasma torque in good agreement with a physics-based model over a wide range of conditions, while first-time main-ion rotation

measurements show it to be lower than expected from neoclassical theory. Core turbulence measurements show increased temperature fluctuations correlated with sharply enhanced electron transport when $\left(\nabla T_e / T_e\right)^{-1}$ exceeds a critical scale length. In H-mode, data show the pedestal height and width growing between ELMs with ∇P at the computed kinetic-ballooning limit, in agreement with the EPED model. Successful modification of a neutral beam line to provide 5 MW of adjustable off-axis injection has enabled sustained operation at $\beta_N \sim 3$ with minimum safety factors well above 2 accompanied by broader current and pressure profiles than previously observed. Initial experiments aimed at developing integrated core and boundary solutions demonstrated heat flux reduction using radiative edges and innovative divertor geometries (e.g., snowflake configuration).

PACS: 52.55.Dy, 52.55.Fa, 52.55.Rk, 52.25.Fi, and 52.25.Xz

1. Introduction

The DIII-D Research Program has made significant advances in developing the physics understanding and operational experience needed to ensure the success of ITER. By simulating candidate operating scenarios in both experiments and modeling with increasing fidelity, this research addresses many of the research needs identified by ITER [1]. Targeted research aims to demonstrate relevant solutions and the scientific basis for avoiding and controlling transient events such as edge localized modes (ELMs) and disruptions which can limit ITER's reliability.

Many of the results reported here capitalize on several new DIII-D capabilities, including variable off-axis neutral beam injection (OANBI) for improved current and pressure profile control, real time steerable electron cyclotron current drive (ECCD) for tearing mode control, high rep-rate pellet injectors, shell pellets, and new diagnostics for validating predictive simulation. These capabilities enable DIII-D to serve as a research platform to qualify advanced operating modes for new superconducting long-pulse tokamaks and for ITER's steady-state mission.

The organization of this paper is as follows. Section 2 summarizes progress on developing ELM control for ITER and how improved understanding of the H-mode pedestal informs the research. In section 3 we discuss progress on disruption mitigation and section 4 covers research in support of the $Q = 10$ ITER mission, including tearing mode control, QH-mode developments, and error field correction. Section 5 covers research directed towards developing predictive capability for burning plasma experiments (pedestal scaling, core transport including intrinsic rotation, and the H-mode threshold). Then in section 6 we discuss results on Advanced Tokamak development

using OANBI, with section 7 providing a description of work producing integrated core-boundary solutions. Future research plans for DIII-D are briefly discussed in the concluding section.

2. ELM Control and the Physics of the Pedestal

ELM control is needed for ITER to achieve its fusion goals without frequent replacement of its divertor components. DIII-D is developing both approaches to ELM control planned for ITER: ELM suppression by application of edge-resonant magnetic perturbations (RMP) [2,3], and pellet pacing [4] to reduce transient heat loads by increasing ELM frequency. In addition, the DIII-D program continues work developing the physics basis for naturally ELM-free QH-mode [5], which may be an attractive operating mode for ITER. QH-mode will be discussed in section 4.

In our most recent experiments, the range in edge safety factor (q_{95}) for RMP ELM suppression was extended to that expected for ITER baseline discharges operating at $q_{95} \sim 3.4$ (note that equilibrium reconstructions without correction for the effect of the finite pressure gradient in the pedestal show $q_{95} \sim 3.1$). Complete ELM suppression was maintained for 3.5 s (~45 τ_E) at ITER relevant pedestal collisionality ($\nu^* \leq 0.1$) with feedback control of the neutral beam heating power keeping $\beta_N > 1.8$ shown in figure 1 [6]. These experiments used an ITER-similar lower-single null shape with $\kappa = 1.8$, $\delta_{up} = 0.4$, $\delta_x = 0.79$ that has the outer divertor strike point positioned to provide particle exhaust with the divertor cryopump (figure 2). The RMP was produced with a single row of internal coils (I-coils) above the plasma midplane to produce $n = 3$ perturbations having a broader range in poloidal mode number m near the internal

resonant surface; previous experiments used both toroidal rows of I-coils (one above and one below the midplane) which produce a narrower spectrum in m that seem to work better at higher q_{95}. However, why this change in spectrum yields ELM suppression at lower q_{95} is not well understood, as SURFMN vacuum calculations show only modest changes to the flux-surface-average resonant components of the applied field going from double rows to a single row of coils. Analysis of the differences when the full plasma response is included is in progress.

To maintain complete ELM suppression for the duration of the discharge, it was important to avoid growth of tearing modes and other internal MHD activity (e.g., fishbones and large sawteeth). This was accomplished using ECCD broadly deposited around the $q = 3/2$ surface [figure 1(c)], though the combined application of the ECCD and RMP caused a significant drop in confinement from $H_{98} \sim 1.1$ to 0.75 in the early H-mode phase of this discharge [figure 1(b)]. In related experiments, ELM suppression with $n = 2$ RMPs at low ITER-like collisionality has also been demonstrated, extending previous results from ASDEX-U showing suppression using $n = 2$ at high collisionality [7].

During initial operations and commissioning of control systems, ITER will use only hydrogen or helium and it will be important for ITER to demonstrate successful operation of its ELM control systems during this initial non-nuclear operating phase. RMP ELM suppression experiments with high fractions of helium (10% to 35%) were carried out using $n = 3$ perturbations in discharges with $q_{95} = 3.4$ and having an ITER similar shape. Complete ELM suppression was only obtained when the helium fraction was less than 25%, possibly due to high collisionality from a lack of density control resulting

from the inability of the divertor cryopump to pump helium. We expect that future experiments using argon-frosting on the divertor cryopump will provide adequate density control with much higher fractions of helium to resolve this issue.

ELM pellet pacing experiments using small (0.9–1.3 mm) deuterium pellets show that the ELM frequency can be increased significantly, producing a corresponding decrease in the measured divertor energy pulse (figure 3). The pellets were injected at a rate of up to 60 pellets/s into an ITER-shaped plasma with $\beta_N = 1.8$ at $q_{95} = 3.5$, achieving up to 12x higher ELM frequency and a strong reduction in impurity content with little impact on core fueling and energy confinement ($H_{98y2} \sim 0.9 - 1.0$). The plasmas were operated near the H-mode power threshold to keep the natural ELM rate (~5 Hz) well below the maximum possible pellet injection rate. In these experiments, three 20Hz pellet injectors were used together to inject 20 pellets/s at ~150 m/s on the low-field side midplane and 20+20=40 pellets/s through the outer scrape-off layer (SOL) just above the X-point (similar to the planned ITER geometry). Significantly, both the peak divertor heat flux measured by IR thermography and total divertor energy pulse (assuming toroidal symmetry) decreases at least as fast as $1/f_{\text{pellet}}$ [4], as shown in figure 4, similar to the usual relation between naturally occurring ELM size and frequency.

The pacing pellets trigger ELMs when they reach no more than half-way into the H-mode pedestal, and high speed imaging of the pellets shows formation of filaments near the pellet, suggesting that ELMs are triggered by local triggering of the instability and not by increasing the density at the top of the pedestal. The observed penetration of the pellets is in agreement with pellet simulations using the JOREK code used to predict pellet penetration in ITER [8].

Extrapolating both pellet pacing and RMP ELM control results to ITER with confidence requires understanding the pedestal structure, its temporal and spatial evolution, and the stability limits that lead to the ELM. The EPED model [9] of pedestal structure provides a conceptual and quantitative framework for developing and interpreting ELM-control experiments. New high repetition rate, high-resolution edge Thomson scattering measurements show how the H-mode pedestal evolves during an ELM cycle (fits to the Thomson data shown in figure 5). Both the pedestal width and pedestal-top pressure grow steadily in time [figure 5(b)], moving along a trajectory of constant pressure gradient that matches the calculated Kinetic Ballooning Mode (KBM) stability limit [10]; fluctuation diagnostics show evidence of high frequency modes in this region with characteristics consistent with KBMs [11]. Comparing calculation and measurement, as in figure 5(b), we observe that when the evolving pedestal crosses the Peeling-Ballooning mode pressure limit, an ELM occurs and the cycle repeats. Thus, mechanisms which prevent the pedestal height or width from growing should, in principle, suppress ELMs. However, unravelling the edge plasma response to applied RMPs in ELM control experiments in order to validate models or improve understanding is challenging due to the steep edge pressure gradients and large magnetic shear in the pedestal region.

Experiments featuring temporal modulation of the $n = 2$ and $n = 3$ RMP toroidal phase and amplitude are providing new insights by comparing changes seen in measurements at different toroidal, poloidal, and radial locations around the tokamak. The data reveal a complex plasma response that includes helical displacements at the edge combined with modulation in the density, temperature, and fluctuation amplitude

near the top of the pedestal where the electron perpendicular drift velocity is zero [6]. New tangential X-point soft x-ray imaging, locked to the RMP toroidal phase modulation shows the existence of filamentary structures or spatial shifts near the separatrix (figure 6), which have been compared to both vacuum-field calculations and two-fluid simulation of the RMP plasma response [12]. The soft X-ray detector has an energy filter which maximizes sensitivity to changes in T_e near the top of the pedestal in the divertor region which occur in phase with changes in RMP phase. Imaging near the x-point provides greater flux-surface resolution due to the large poloidal flux expansion near the field null. As shown, simulations which include two-fluid plasmas response are in better qualitative agreement with measurements than are vacuum field calculations. We also find that the edge density response to the RMP is nearly independent of q_{95}, while the edge T_e responds most strongly when q_{95} is within the suppression window. With RMP amplitude modulation, long wavelength $\left(k_\perp \rho_i < 1\right)$ density fluctuations around r/a~0.9 increase rapidly as the RMP amplitude rises, followed by changes in the local density, suggesting that RMP changes density by changing turbulent transport [13]. Overall, the full suite of observations is consistent with the picture that the RMP generates a strong resonant response near the top of the pedestal, where the electron drift frequency is near zero ($\omega_{*e} \sim 0$), increasing transport to limit the pedestal width to remain below the Peeling-Ballooning limit, thereby averting the ELM.

3. Disruption Mitigation

Disruptions in ITER are expected to generate large runaway electron (RE) currents compared to present tokamaks (up to 70% of the initial current, or up to 10 MA for a 15

MA ITER discharge) [14]. While massive gas injection (MGI) will mitigate the thermal quench, it will be far more challenging for MGI to prevent REs by raising density to the so-called "Rosenbluth density" [15] in ITER. Experiments in DIII-D using either MGI, shattered argon pellets, or boron-filled shell pellets have so far reached only ~20% of the scaled target value [16], with the possibility of further increases looking uncertain. Even so, MGI at present assimilation levels can significantly reduce the potential damage from RE in ITER by dramatically increasing runaway electron dissipation should their current be significant.

Systematic study of RE dynamics and dissipation in DIII-D shows that passively stabilized high-current ($I_{RE} < 0.6$ MA), high energy (~20 MeV) RE beams dissipate benignly against the inner wall while drifting vertically over many milliseconds, smoothly decaying from the outside-in until the innermost energetic core (~0.3 m diam.) is finally in contact with the wall [17]. Figure 7(a) shows synchrotron emission for RE in DIII-D formed during the current quench in a triggered disruption. When formed, the most energetic RE exist only in the very core of the residual current channel. About 50 ms later, after the total RE current has decreased to 10%–20% of its initial value, the hot core begins interacting more strongly with the inner wall. At this point, wall impurities increase rapidly causing the RE beam to disrupt; data shows most of the residual magnetic energy is then safely converted to a current of low energy electrons which hit the wall without damage. No significant damage has been observed even after many such disruptions producing significant RE currents, reflecting both the benign termination process and the lack of large toroidal gaps or protruding surfaces and components inside DIII-D.

High-Z impurity gas injection (argon and neon) during [figure 7(b)] or after RE [figure 7(c)] formation strongly increases the dissipation rate, in some cases allowing complete benign dissipation of up to 600 kA RE beams even without active position control. With active position control, the RE beam current ($I_{RE} \leq 300$ kA) can be maintained out to the V-S limit of the ohmic solenoid or until the current is smoothly ramped to zero, allowing precise loop voltage, electric-field, impurity spectroscopy, and density measurements under a variety of conditions [18] that enable comparison between measured and predicted dissipation rates. Overall, the dissipation rate is as much as 10x higher than expected from e-e collisions only, and the measured RE energy distribution shows a much larger fraction of lower-energy electrons than expected from avalanche theory and e-e collisions alone [16]. These results suggest that prompt massive injection of high-Z impurity atoms at the current quench, reaching total (bound+free) electron densities well below the Rosenbluth density, may provide a reliable means for safely dissipating large runaway electron currents without damage to internal components in ITER.

Other disruption mitigation studies systematically examined the first-wall heat flux resulting from vertical displacement events (VDEs) in single-null discharges. High speed IR TV measurements showed that most of the heat flux was deposited on the inner wall near the divertor, independent of toroidal field direction; low shot-to-shot variation implies less than 30% toroidal variation. Prompt argon injection at the start of the thermal quench reduced the divertor heat flux by 40%, though little reduction was observed if delayed by 25 ms.

4. Meeting ITER Performance Goals in the Burning Plasma Regime

The DIII-D research program places high priority on experiments which simulate planned ITER operating scenarios, matching shape, β_N, collisionality (ν^*), and rotation. Rotation is particularly important because of its significant impact on confinement and stability. Furthermore, due to its large moment of inertia, ITER will have low externally driven rotation compared to present tokamaks which have significant neutral beam heating. Plasma rotation in DIII-D can be controlled by varying the mix of co-I_p (15 MW) and counter-I_p (5 MW) neutral beam injection torque and power. The scaled ITER equivalent NBI torque ($T_{NB,D3D}^{equiv}$) is defined as that which would produce the same rotation in DIII-D as would NBI torque in ITER ($T_{NB,ITER}$). Assuming $\Omega = T\tau_L / I_{plasma}$ and the angular momentum confinement time (τ_L) varies linearly with the energy confinement time in each tokamak, using the moment of inertia (I_{plasma}) computed from the density profile with transport codes we obtain

$$T_{NB,D3D}^{equiv} = T_{NB,ITER} \frac{I_{D3D}\tau_{E,ITER}}{I_{ITER}\tau_{E,D3D}} \cong 0.3 - 1.0 \text{ N} - \text{m} \quad , \tag{1}$$

depending on discharge conditions. Further details are provided in the Appendix of Ref. 19.

The importance of external NBI torque and resulting rotation is illustrated by the sensitivity of low-torque discharges to tearing modes, which reduce confinement and can lock to low-n field errors to produce a disruption. With strong co-current neutral beam injection, and feedback controlled $\beta_N \sim 2$, ITER-shaped plasmas at $I/aB = 1.4$ reached and maintained stationary conditions with $H_{98y2} > 1$, $\ell_i \sim 0.8 - 0.9$, and free of tearing

modes for $>10\tau_R$. However, small changes in β or a small reduction in co-current NBI torque and plasma rotation resulted in increased tearing mode activity. Adding ~3 MW of ECCD broadly deposited near the $q = 3/2$ surface (~30 kA total current drive) suppressed the tearing modes even as the NBI torque was reduced to the scaled ITER equivalent of <1 Nm, allowing stationary conditions to be maintained for more than four resistive times [20] (figure 8). Subsequently, long-pulse ITER baseline scenario demonstration discharges featuring low-torque start up and ramp up were obtained.

Successful low-torque ramp up to stationary conditions simulating the ITER hybrid or advanced inductive (AI) scenario, has been demonstrated [21]. This scenario features higher β operation with improved stability at higher q_{95} (i.e., lower current) than the ITER baseline case. Equivalent stationary conditions were obtained by either ramping up β_N at constant torque following low-torque start up or by ramping down torque and rotation at constant β_N after start up with significant NBI torque. Reducing the NBI torque and plasma rotation reduced energy confinement significantly (H_{98y2} dropped from 1.5 typical of our best AI plasmas to 1.0) in either case. Once stationary, these discharges operated at $\beta_N \sim 3$, $H_{98y2} \sim 1$, $q_{95} \sim 4$, obtaining equivalent fusion gain $G = \beta_N H_{89} / q_{95}^2 \sim 0.35$, nearing that expected for ITER $Q = 10$ operation ($G = 0.4$). Similar to the ITER baseline scenario experiments described above, at reduced torque the plasma becomes more susceptible to neoclassical tearing modes which generally slow and lock. Application of ~1 MW of ECCD or ECH near or even inside the $q = 2$ surface suppressed these modes, allowing stable high performance operation ($\beta_N \sim 2.5$) even with zero net NBI torque and very low plasma rotation.

Research continued on developing the physics basis for another promising ITER operating mode, the ELM-free QH-mode [5]. Recent experiments using only external coils (*outside the toroidal field coils*) have produced stationary QH-mode discharges with low plasma rotation, extending the operating space to include co-current NBI torque providing 3–4 times the torque scaled from the ITER beams [22]. The strong edge rotational shear needed for QH-mode access was maintained using counter-I_p torque arising from neoclassical toroidal viscosity (NTV) [23] produced by applying non-resonant magnetic fields (NRMF). Best results have been obtained with $n = 3$ external coils, though $n = 3$ NRMF using internal coils also works well.

These QH-mode plasmas exhibit excellent confinement at low rotation with low NBI torque ($H_{98y2} = 1.3$), as shown in figure 9, and in contrast to ELMing H-modes at low rotation. They operate stably at $\beta_N \sim 2$ with low collisionality $\nu^*_{ped} = 0.05$ at $q_{95} = 4.7$ $(I/aB = 1.05)$ with nearly zero core rotation [24]. Higher current discharges with $G = 0.4$ have been obtained at $q_{95} = 3.4$ as well. The fact that QH-mode can be obtained robustly over a wide range in heating power using NRMF to produce the rotational edge shear may make it an attractive operating mode for ITER.

ITER may be susceptible to tearing modes if the plasma rotation is small or fast-ion-stabilized sawteeth grow to large amplitude during the fusion burn. Therefore, ITER plans to have active neoclassical tearing mode (NTM) control.

Improved neoclassical tearing mode (NTM) control integrating all the elements of NTM control for ITER is now available on DIII-D. Actively tracking the $q = 2$ and/or $q = 3/2$ surfaces and applying ECCD when NTMs are first detected reduces the power required to suppress tearing modes altogether, confirming the feasibility and benefit for

such feedback control in ITER. Several integrated control schemes have been developed and tested, which combine real-time motional Stark effect (MSE) measurements to locate the target q-surface, fast steering mirrors on the EC launchers to adjust the deposition location, a model-based aiming algorithm which corrects for beam diffraction in the plasma [25], and reliable methods to detect the NTM. Both 3/2 and 2/1 neoclassical tearing modes have been suppressed (2/1 suppression shown in figure 10), with significantly more power required to suppress the 2/1 mode than the 3/2 mode, as expected from its larger growth rate and the requirement that the EC driven current must be greater than the missing local bootstrap current at the mode-rational surface [26]. Early ECCD application significantly reduces the power required for suppression to well below 0.5 MW for the 3/2 mode. In extreme cases where the tearing mode grows large enough to lock, experiments have shown that 3D field coils can be used to align the toroidal location of the O-point with ECCD deposition to stabilize the mode and avoid disruption [27].

Since disruptive tearing modes can also be destabilized by large fast-ion stabilized sawteeth, we have carried out experiments to stabilize such modes. In ELMing H-mode discharges, ECCD was used to increase the magnetic shear near the $q = 1$ surface and reduce the size of such fast-ion stabilized sawteeth oscillations, thereby allowing operation at $\beta_N > 3$ without large 2/1 tearing modes [28], an important demonstration of the physics basis for this approach in ITER.

Large, uncorrected non-axisymmetric residual magnetic fields (e.g., $n = 1$ error fields) are deleterious to tokamak performance, in the worse case leading to locked modes and plasma disruptions. In larger devices with potentially lower rotation, such as

ITER, the plasma becomes less tolerant to error fields and improved error-field compensation will be required [29].

Error field correction experiments utilizing large proxy $n = 1$ error fields from either external coils or the ITER Test Blanket Module (TBM) mock-up coil [30] show that correcting only the lowest-order error field components can introduce strong residual rotational drag which reduces stability and confinement. The TBM mock-up coil introduced a highly localized field perturbation at a single toroidal location, while the external C-coils [figure 11(a)] created a more purely $n = 1$ error field without higher order harmonics. Two toroidal rows of six internal coils (the I-coils) provided the error field correction (EFC) in each case [31]. In the TBM experiments, the toroidal rotation of the plasma with constant neutral beam torque was used to infer the change in torque on the plasma from the error fields with and without error field correction; application of $n = 1$ EFC restored only ~25% of the drop in rotation observed when the TBM coils were activated [32]. In the C-coil error field experiment, the effect of EFC was determined by its impact on the low density locked-mode threshold; only modest improvement was observed when using $n = 1$ EFC to correct the n=1 error field. Modeling with the IPEC code explained the results for this $n = 1$ proxy error field experiment [33] through an increase in non-resonant fields and rotation braking when the low-order resonant correction was applied [figure 11(b)].

These results confirm present understanding that error field correction strategies must include the full plasma response of all the field components to determine the best coil combinations for correction [33]. This suggests that optimal correction may require ITER to maintain flexibility in its EFC coil set to produce multiple poloidal harmonics, possibly

including its ELM control coils in the mix while using measured plasma rotation to provide feedback control for optimizing the correction.

5. Developing Predictive Capability for Burning Plasma Experiments

It is important to develop validated predictive models for ITER to guide design choices, help determine operational requirements, and inform experimental planning once ITER is operational. Informed planning will enable most efficient use of the facility and maximize progress toward fusion energy. Fusion gain depends on the global energy confinement, which in H-mode is determined by the combined effects of stability and transport in the core and edge pedestal regions. Validated transport models are needed for both and have been the subject of recent joint experiments involving DIII-D, NSTX, and Alcator C-Mod [34,35].

The DIII-D program carried out experiments to measure core transport stiffness in L-mode and H-mode discharges, and to further explore the theory-measurement discrepancy in L-mode edge transport at $\rho \geq 0.7$. Stiffness refers to a sharp increase in transport when the temperature gradient exceeds a critical value; high stiffness in H-mode implies that the core profile simply rides on top of the pedestal, yielding $P_{\text{fusion}} \propto \beta_{\text{pedestal}}^2$. It is important to examine transport and stiffness in L-mode as well as H-mode, because L-mode transport impacts the plasma current during the initial I_p ramp and H-mode access.

The critical gradient scale length for the onset of increased electron transport in L-mode discharges was measured using localized electron cyclotron heating (ECH) to vary the gradient scale lengths at the plasma mid-radius by over factor of 4 while

changing the local heat flux in small steps by a factor of 10, as shown in figure 12. Measurements were obtained with and without co-, counter- and balanced-I_p NBI heating. Both power balance and heat pulse propagation showed similar responses, consistent with a sharp rise in transport when the gradient scale length $1/L_{T_e} = \nabla T_e/T_e > 3.0\ \mathrm{m}^{-1}$ [36,37], [figure 12(b)]. During these experiments, a sharp rise in local electron temperature fluctuations and a change in the $\tilde{n}\tilde{T}_e$ cross-phase co-incident with the change in transport was observed for the first time [figure 12(c)], using correlation electron cyclotron radiometry [38].

The sharp rise in T_e fluctuations indicates that trapped electron modes are becoming important, providing an excellent test for gyrokinetic simulations. Both TGLF and nonlinear GYRO simulations show the sharp rise in thermal transport, Q_e, above the critical gradient [figure 12(b)] though the electron heat flux in GYRO appears to saturate at much lower value than either experiment or TGLF [35]. GYRO shows the T_e fluctuations should increase with higher gradients although the fluctuation levels are lower than observed in this experiment.

In separate beam-heated H-mode discharges, no sign of a critical gradient threshold for increased ion or electron transport is observed, possibly because low values of ∇T could not be accessed. These experiments examined both co-I_p and balanced NBI heating, varying beam power by a factor of three (3.3 to 9.2 MW). The discharges were designed to minimize changes in the pedestal conditions by operating at low triangularity, though in fact the pedestal β rose with heating power, in contrast to assumption of fixed pedestal pressure typical of many core transport simulations. The results of the

experiment show that, inside $\rho \sim 0.5$, electron thermal transport is stiffer than ion, while at larger ρ the stiffness is similar on (figure 13), in agreement with both TGLF and full gyrokinetic simulations (solid lines) using the measured pedestal parameters at $\psi_N = 0.85$ [35] as the boundary conditions.

Other transport experiments yielded fluctuation measurements which may point to an explanation of the shortfall in gyrokinetic simulations of L-mode edge transport as compared to experiment in the outer part of the plasma (for $\rho \geq 0.7$). Data at lower current (higher q_{95}) show increased edge temperature and density fluctuations with a concomitant decrease in low frequency turbulent flow, as compared to the lower q_{95} companion case [39]; correlating large changes in both the shortfall and the turbulence with changes in the magnetic shear should help identify the physics changes required to improve the fidelity of simulations.

Core transport and stability are strongly affected by plasma rotation and rotational shear, which must be included in transport models. It is straightforward to calculate the torque on the plasma from neutral beam injection, but the intrinsic torque arising from neoclassical and other transport effects is not well documented. Using co- and counter-NBI to apply a step change in NBI torque, the intrinsic torque as a function of radius has been inferred from the changes in the rotation profile, and from these data a simple physics-based model of intrinsic rotation has been developed. In the edge pedestal region, data show that turbulent Reynolds stress alone is insufficient to explain the formation of a large intrinsic edge rotation layer. A model which includes edge thermal-ion orbit loss $\left(\propto \sqrt{T_i}\right)$ and ∇P_{ped} describes measured intrinsic edge torque in DIII-D and NSTX H-mode plasmas, including Advanced Inductive discharges with much higher intrinsic

torque [40]. This model predicts a relatively low intrinsic torque of only 2 N-m in ITER (figure 14), as compared to 35 N-m provided by the neutral beams, which implies that rotation in ITER may be small due to its large moment of inertia.

The study of plasma rotation and transport benefits from first-time simultaneous measurements of main ion and impurity ion (carbon) rotation profiles. With low external torque, flow shear will largely depend on ∇P and poloidal flow velocity. The new measurements [41,42] show anomalously large main-ion poloidal rotation at low collisionality ($\nu^* < 0.1$) in low-torque H-mode discharges, as compared to the usual inference of main-ion flow velocity from charge exchange recombination measurements of carbon. These results may have implications for transport in ITER, where toroidal rotation may be reduced.

Fast-ion transport is a key element to achieving fusion gain. The ability to vary the fast-ion pressure profile and the fraction of trapped/passing ions using off-axis NBI, coupled with a comprehensive diagnostic set, provides an excellent set of tools for exploring fast-ion physics in DIII-D. Using off-axis injection to vary the fast ion pressure gradient ($\nabla\beta_f$) near $q_{\min}$, where reversed-shear Alfvén Eigenmodes (RSAEs) are unstable, shows stabilization of RSAEs as the OANBI reduces $\nabla\beta_f$, as expected [43,44]. In related studies, we find that resistive wall mode (RWM) stability is improved by off-axis beam injection [45]. Finally, in another important test of fast-ion physics, the fast-ion losses produced by the DIII-D ITER TBM mock-up coil were measured using an infrared camera, and the data compared with predictions from four different orbit-following simulation codes for cases with a wide variety of EP sources (co-counter and on-off axis NBI). Results show that vacuum field calculations are sufficient to calculate the EP losses

and that plasma response plays at most, only a minor role in prompt loss of these fast ions [46].

The relatively good agreement between TGLF transport simulations and H-mode data relied in part on using the measured pedestal parameters as a boundary condition for the core plasma. So predicting the temperature at the top of the pedestal is a key element in building a robust scientific basis for the H-mode confinement database used to predict performance in ITER [47]. Coordinated experiments involving DIII-D, C-Mod, and NSTX produced high-resolution edge pedestal profile data which were compared against a number of theory-based simulation codes [34]. Adding the data from C-Mod doubled the range over which the EPED model correctly predicts the pedestal height without recourse to adjustable or fitted parameters. With the present database growing to 270 discharges from 5 tokamaks (figure 15), there is increased confidence that the EPED model can be used to predict the pedestal pressure height in ITER to within ~20%, using MHD and kinetic stability calculations and incorporating no fitted parameters. Significantly, the predicted value matches the expectation for achieving $Q = 10$ H-mode operation in ITER. This model also guides ELM mitigation experiments with RMPs and pellets, and is consistent with interpretation of ELM-free QH-mode operation.

Obtaining the benefit of H-mode confinement naturally requires H-mode access. However, the trigger for the L-H transition has remained elusive even though the paradigm of flow-shear stabilization of edge turbulence following the H-mode transition is well documented. Recent diagnostic developments have provided significantly improved temporal resolution for turbulence and turbulent flow measurements are

possibly revealing the underlying physics of the transition threshold for the first time [48].

In DIII-D, near the H-mode power threshold, so-called "dithering" H-mode transitions exhibit limit-cycle oscillations are observed, which allow study of the transition dynamics on an expanded timescale, as illustrated by the variation in H_α emission shown in figure 16(a) as the plasma transitions from L-mode to H-mode confinement. Microwave Doppler Backscattering (DBS) measures the both amplitude of high frequency density fluctuations and mean $E \times B$ flow near across a region around the separatrix with high temporal resolution. DBS data from a single 3ms limit cycle, shown in figure 16(b) illustrate the predator-prey dynamics going from high $\tilde{n}/n$ and low $v_{\mathrm{E\times B}}$ and back again; eventually the pressure-gradient driven flow shear locks in the H-mode with high flow shear and low fluctuations [49,50].

Related studies of the L-H transition using beam emission spectroscopy (BES) show trends in turbulence and turbulent flows at the H-mode transition that mirror well-known density and magnetic field scaling of the H-mode power threshold [51]. Just prior to the transition, the data show reduced high frequency (20–150 kHz) fluctuation amplitudes near the separatrix at higher toroidal field, suggesting a reduced drive for zonal flows, while BES velocimetry measurements shows low frequency turbulent flow velocity shear increasing at lower density. Both trends are consistent with the observed scaling in H-mode power threshold $\left(P_{\mathrm{LH}} \propto n^{0.7} B^{0.8}\right)$. DIII-D H-mode transition data have also been incorporated into an updated multi-machine database [52].

6. Research on the Path to Fusion Energy: High-β Steady-State Operation

Significant off-axis current drive capability has been added to DIII-D in order to evaluate advanced configurations having broad current and pressure profiles capable of high β_N fully noninductive steady-state tokamak operation [53]. Theory and experiment indicate that broad current profiles peaked off-axis are beneficial for steady state high performance solutions. This line of research supports both the ITER steady-state mission and future tokamak development.

Successful modification of a DIII-D neutral beam line now provides capability for up to 5 MW of adjustable off-axis co-current NBI (OANBI) out of 20 MW maximum total NBI power. The adjustment is accomplished [54] by tilting the back end of the degree beam line vertically upward about a pivot point located in the beamline drift duct at the plasma midplane. The injection poloidal tangency radius is adjustable during a single experimental day over the range $0 \le \rho \le 0.5$ for full-size plasmas ($a \sim 0.62$ m). The grid structures and collimating apertures for the two sources in the beamline were modified to reduce interaction with the side of the tokamak entrance port. The aiming and positioning of the neutral beams was checked at the start of tokamak operation using H_α visible imaging and beam-dump heat flux measurements [55], as shown in figure 17(a,b). Measurements comparing D-D neutron production, fast ion profiles, and plasma heating indicate that the source and beamline modifications have reduced the heating power by ~15%–20% compared to the previously unmodified beam operating at similar parameters, independent of the tilt angle.

Comprehensive measurements show that off-axis neutral beam current drive and fast ion transport agree with numerical simulation [56]. The neutral beam current drive is very

sensitive to toroidal field direction, which significantly changes the ratio of trapped to passing particles; "reversed" B_T (I_p and B_T in the same direction) provides 45% more current drive and peaks the current further off axis. Figure 17(c) shows the NBI current drive due to off-axis as compared on-axis current drive derived from MSE-constrained equilibrium reconstruction; there is good agreement in shape and magnitude with NUBEAM simulation. More extensive studies show no degradation in current drive due to microinstabilities as β increases [56].

The off-axis current drive capabilities enable access to a new range of profiles with sustained minimum safety factors $q_{\min} > 2$, for durations greater than 2 s [57], as shown in figure 18. These high-$q_{\min}$ plasmas operating at $B_{\text{tor}} = 1.8$ T maintain $\beta_N \sim 3$, well below the calculated beta limit $(\beta_N > 4)$. Because $q_{\min} > 2$, there are no deleterious 2/1 and 3/2 tearing modes, although higher order modes do appear, often as q passes through a rational value; if such modes persist, they produce a small decrease in confinement (~15%). These discharges using off-axis injection are not limited by stability, but rather by available heating power and somewhat reduced confinement. Because we are seeking to maximize the noninductive current fraction in our steady-state research, we do not use counter NBI, which limits the input power to ~15 MW. In addition, although H_{98y2} is still $\gtrsim 1$, this value is typically ~20% lower than comparable discharges with on-axis injection and lower $q_{\min}$; an observed increase in Alfvén mode activity might be a contributing factor.

Off-axis injection produces both broader current profiles (lower ℓ_i) and broader pressure profiles $\left[P(0)/\langle P\rangle \leq 3\right]$ than previously sustainable, as in figure 19. Both factors should produce significantly higher ideal stability limits than previously obtainable under

stationary conditions; DCON calculations of the ideal-wall $n = 1$ β_N limit carried out using measured profiles show that off-axis injection does indeed produce more discharges with higher beta limits than does on-axis injection (figure 20). Discharges with calculated β_N limits >4.0, indicated by the red symbols in the figure, are most commonly obtained with off-axis injection (box + symbols), in contrast to discharges with on-axis injection (+ symbols only) which generally yield β_N limits <4.0 (blue symbols).

Relaxing $q_{\min}$ to 1.5 leads to steady-state discharges with improved confinement at $\beta_N = 3.5$ that are close to meeting the requirements for steady-state $Q = 5$ operation in ITER and also for FNSF-AT operating at $Q \sim 4$ [58]. The DIII-D discharges have high noninductive current fractions, $f_{NI} \sim 0.7$, and are maintained free of low-order tearing modes by OANBI and ECCD for two current profile relaxation times ($2\tau_R = 3$ s), limited by available beam energy (power and pulse length), as shown in figure 21. The ECCD (3.2 MW) was applied steadily at $\rho \sim 0.4$ and dynamic error field correction was also used. The safety factor (both $q_{\min}$ and ρ_{qmin}) and pressure profiles generally agree with FASTRANS simulations [56] that incorporate TGLF transport simulations and realistic heating and current drive inputs. Modest differences that are observed between simulation and experiment in $T_e(0)$ (20% higher than measured) and mid-radius T_i profile (steeper computed ∇T_i across $\rho \sim 0.2 - 0.3$) can be reduced by increasing the fast-ion diffusion coefficient in the core, possibly due to the observed increase in Alfvén eigenmode activity noted earlier.

7. Research on the Path to Fusion Energy: Integrated Core-Boundary Solutions

Future steady state fusion devices will place higher demands on plasma facing components, and new integrated core-edge-divertor solutions will be needed. Initial integration experiments have used neon injection to enhance edge and divertor radiation in the high β_N steady-state discharges described in section 6. Neon injection in the divertor of these Advanced Tokamak discharges ($\beta_N = 3$ and $q_{min} = 1.5$) doubled the radiative loss from the edge and divertor without degrading confinement ($H_{89p} = 2.4$), reducing peak divertor heat flux by ~40%. Eventually, steady neon puffing caused a radiative collapse, so future experiments will utilize divertor pumping and feedback control to limit the neon content and total radiative loss to maintain good confinement.

Very promising results were obtained using the snowflake (SF) divertor configuration to reduce the peak heat flux as compared to a standard single-null divertor. Using only the external poloidal field coils, SF divertor configurations [59], such as the Snowflake-minus in DIII-D (figure 22) can provide much larger SOL volume near the X-point, larger divertor contact area in the SOL adjacent to the separatrix (3–4x), and longer parallel connection length than a standard divertor, especially below the X-point, where the plasma, neutral gas, and impurity densities are high. The Snowflake-minus configuration shown in figure 22 has two null points, with the one near the outer divertor target producing very large local flux expansion. Data from an ELMing H-mode discharge, figure 23, show that the increased flux expansion lowers the peak divertor heat flux by about a factor of three. Early analysis of a limited number of SF-minus discharges indicates that the energy loss per ELM and resulting peak divertor ELM heat flux also are significantly reduced [60]. Deuterium gas injection in the divertor region leads to divertor

detachment at similar line-average density as in the conventional divertor, though the radiative volume appears larger (figure 24); in this detached state both the steady-state and transient ELM heat pulses are eliminated, as shown.

Understanding the magnitude of the divertor challenge is a necessary component in the development of suitable plasma-based solutions. Joint experiments between DIII-D, C-Mod, and NSTX have produced a coordinated multi-machine database relating measured divertor heat flux profiles to H-mode edge pedestal parameters over a wide range of conditions [61]. Analysis shows the peak divertor heat flux scaling as $P_{\mathrm{SOL}}^{1.2} B_{\mathrm{tor}}^{-0.3} B_{\mathrm{pol}}^{-1}$ where P is the SOL power and B_{pol} is the midplane poloidal field at the separatrix [62]. These data were recently combined with data from JET and ASDEX [63] to form a more comprehensive database that confirms this trend, suggesting a much higher parallel SOL heat flux ($\lambda_q \sim 1$ mm) than previously expected in ITER ($\lambda_q > 5$ mm). However, this extrapolation to a very small λ_q in ITER looks to yield pressure gradients near the midplane separatrix which exceed expected edge-pedestal stability limits, suggesting that such a simple extrapolation to ITER may not hold and that λ_q will be significantly larger [62].

The all-carbon plasma facing components in DIII-D make it possible to measure the gross and net surface erosion rates of tungsten in the divertor under realistic conditions using the DiMES divertor material exposure system. By exposing well-characterized tungsten samples in DIII-D ELMing H-mode plasmas and measuring the change in areal surface density of tungsten, it was possible to determine both the total sputtering and net erosion from the sample, as well as the amount of tungsten redeposited nearby. The data

shows that the bulk of the sputtered tungsten was promptly deposited [64], in agreement with DIVIMP simulation and consistent with expected lifetime in ITER.

8. Summary and Future Plans

In this paper we have described recent DIII-D research in a number of areas pertinent to successfully completing design, construction, and operation of ITER, and which support the development of steady-state tokamak reactors.

Prototype $Q = 10$ ITER discharges in DIII-D with low applied torque show that achieving required performance is possible while using active feedback ECCD for tearing mode control. Advances in pellet pacing and RMP physics move these ELM control techniques closer to ITER design requirements while strengthening the physics basis for their application; high confinement ELM-free QH-mode can now be obtained over a wide range of applied NBI co-and counter-I_p torque using external $n = 3$ coils. Disruption mitigation experiments point to the possibility of benign runaway electron dissipation with massive gas injection even when well below the Rosenbluth limit.

DIII-D experiments continue to advance the scientific basis to fully exploit ITER by increasing predictive capability for further optimization. Many aspects of the EPED model describing the H-mode pedestal have been confirmed and are now informing ELM control experiments. Deployment of a comprehensive set of fast-ion diagnostics, along with OANBI and new 2D fluctuation measurements, has enabled comprehensive tests of simulation codes that will be used to interpret fast-ion stability and transport in ITER.

Off-axis neutral beam injection is providing new capability for advancing research aimed toward steady-state high-beta Advanced Tokamak operation needed for fusion

energy development. Such operating modes are envisioned for ITER and could form the basis of a future Fusion Nuclear Science Facility (FNSF-AT) [58]. Off-axis neutral beam injection has enabled operation with $q_{\min} > 2$ to avoid the most unstable tearing modes, measurably broadened the current profile, and sustained high β discharges for more than twice the current relaxation time. In parallel, DIII-D is exploring innovative divertor solutions to address the challenge of steady-state power and particle control.

Future plans seek increased EC power for heating and current drive to improve access to regimes with dominant electron heating, and to improve capability for developing steady-state operating regimes for long-pulse superconducting tokamaks and burning plasma experiments. Commissioning of a 7th long-pulse gyrotron is now under way, with proposed installation of two additional gyrotrons by 2014 to provide increased ECCD power. Other upgrade plans call for additional 3D coil sets and related power supplies in following years. Ongoing modification of existing neutral beam lines to allow longer pulse lengths will continue in the near term. In the future, we plan to tilt a second beam line to increase capability for Advanced Tokamak research.

Acknowledgment

This work was supported by the US Department of Energy under DE-AC52-07NA27344 and DE-FC02-04ER54698.

References

[1] Campbell, D.C., https://burningplasma.org/ref/ITPACC_campbell_dec11.pdf

[2] Evans, T.E., *et al*. 2004 *Phys. Rev Lett*. **92** 235003

[3] Evans, T.E., Orlov, D.M., Wingen, A., Wu, W., Loarte, A., Casoer, T.A., Schmitz, O., Saibene, G., and Schaffer, M.J., *IAEA, Proc. of the 24th IAEA Fusion Energy Conf. (San Diego, CA, 2012)* Paper ITR/P1-25

[4] Baylor, L.R., *et al*., *IAEA, Proc. of the 24th IAEA Fusion Energy Conf. (San Diego, CA, 2012)* Paper EX/6-2

[5] Burrell, K.H., *et al*. 2001 *Phys. Plasmas* **8** 2153

[6] Wade, M.R., *et al*., *IAEA, Proc. of the 24th IAEA Fusion Energy Conf. (San Diego, CA, 2012)* Paper EX/3-1

[7] Suttrop, W., *et al*. 2011 *Phys. Rev. Lett*. **106** 225004

[8] Futatani, S., Huijsmans, G., Loarte, A., Baylor, L.R., Commaux, N., Jernigan, T.C., Fenstermacher, M.E., Lasnier, C.J., Osborne, T.H., and Pegourié, B., *IAEA, Proc. of the 24th IAEA Fusion Energy Conf. (San Diego, CA, 2012)* Paper ITR/P1-22

[9] Snyder, P.B., Osborne, T.H., Burrell, K.H., Groebner, R.J., Leonard, A.W., Nazikian, R., Orlov, D.M., Schmitz, O., Wade, M.R., and Wilson, H.R., 2012 *Phys. Plasmas* **19** 056115

[10] Snyder, P.B., *et al*., *IAEA, Proc. of the 24th IAEA Fusion Energy Conf. (San Diego, CA, 2012)* Paper TH/P3-17

[11] Gao, L., Balakrishnan, Sreenath, He, Weikai, Yan, Zhen, and Müller, Rolf, 2011 *Phys. Rev. Lett*. **107** 214301

[12] Ferraro, N.M., Lao, L.L., Evans, T.E., Moyer, R.A., Nazikian, R., Orlov, D.N., Shafer, M.W., and Unterberg, E.A., *IAEA, Proc. of the 24th IAEA Fusion Energy Conf. (San Diego, CA, 2012)* Paper TH/P4-21

[13] McKee, G.R., *et al.*, *IAEA, Proc. of the 24th IAEA Fusion Energy Conf. (San Diego, CA, 2012)* Paper EX/P7-06

[14] Hender, T.C., *et al.*, Nucl. Fusion **47** 095003 (2007)

[15] Rosenbluth, M.N. and Putvinski, S.V. 1997 *Nucl. Fusion* **37** 1355

[16] Hollmann, E.M., *et al.* 2011 *Nucl. Fusion* **51** 103056

[17] Hollmann, E.M., *et al.*, *IAEA, Proc. of the 24th IAEA Fusion Energy Conf. (San Diego, CA, 2012)* Paper EX/9-2

[18] Eidietis, N.W. 2012 *Phys. Plasmas* **19** 056109

[19] Garofalo, A.M., *et al.* 2011 *Nucl. Fusion* **51** 083018

[20] Jackson, G.L., *et al.*, *IAEA, Proc. of the 24th IAEA Fusion Energy Conf. (San Diego, CA, 2012)* Paper EX/P2-08

[21] Solomon, W.M., *et al.*, *IAEA, Proc. of the 24th IAEA Fusion Energy Conf. (San Diego, CA, 2012)* Paper EX/P2-01

[22] Burrell, K.H., K.H., Garofalo, A.M., Solomon, W.M., Fenstermacher, M.E., Osborne, T.H., Park, J.-K., and Snyder, P.B., *IAEA, Proc. of the 24th IAEA Fusion Energy Conf. (San Diego, CA, 2012)* Paper EX/P4-08.

[23] Cole, A.J., Hegna, C.J., and Callen, J.D. 2007 *Phys. Rev. Lett.* **99** 065001 and references therein

[24] Garofalo, A.M., Burrell, K.H., Solomon, W.M., Fenstermacher, M.E., Hanson, J.M., Lanctot, M.J., Okabayashi, M., Snyder, P.B., and the DIII-D Team, *EPS,*

Proc. of the 39th Conf. on Plasma Physics, (Stockholm, SE, 2012) Paper O2.102; http://ocs.ciemat.es/epsicpp2012pap/html/author.html

[25] Kolemen, E., Welander, A.S., La Haye, R.J., Eidietis, N.W., Humphreys, D.A., Lohr, J., Noraky, S., Penaflor, B.G., Prater, R., and Turco, F., "State-of-the-Art Neoclassical Tearing Mode Control in DIII-D Using Real-time Steerable Electron Cyclotron Current Drive Launchers," *IAEA, Proc. of the 24th IAEA Fusion Energy Conf. (San Diego, CA, 2012)* Post-deadline submission

[26] Nagasaki, K., Isayama, A., Ide, S., and JT-60 Team 2003 *Nucl. Fusion* **43** L7

[27] Volpe, F.A., Austin, M.E., La Haye, R.J., Lohr, J., Prater, R., Strait, E.J., and Welander, A.S. 2009 *Phys. Plasmas* **16** 102502

[28] Chapman, I.T., *et al.*, *IAEA, Proc. of the 24th IAEA Fusion Energy Conf. (San Diego, CA, 2012)* Paper ITR/P1-31

[29] Buttery, R.J., *et al.* 2011 *Nucl. Fusion* **51** 073016

[30] Schaffer, M.J., *et al.* 2011 *Nucl. Fusion* **51** 103028

[31] Buttery, R.J., *et al. IAEA, Proc. of the 24th IAEA Fusion Energy Conf. (San Diego, CA, 2012)* Paper EX/P4-31

[32] Reimerdes, H., *et al. IAEA, Proc. of the 24th IAEA Fusion Energy Conf. (San Diego, CA, 2012)* Paper EX/P4-09

[33] Buttery, R.J., *et al.* 2012 *Phys. Plasmas* **19** 056111

[34] Groebner, R.J., *et al. IAEA, Proc. of the 24th IAEA Fusion Energy Conf. (San Diego, CA, 2012)* Paper EX/11-4

[35] Holland, C., *et al. IAEA, Proc. of the 24th IAEA Fusion Energy Conf. (San Diego, CA, 2012)* Paper EX/P7-09

[36] Luce, T.C., *et al*. *IAEA, Proc. of the 24th IAEA Fusion Energy Conf. (San Diego, CA, 2012)* Paper EX/P3-18

[37] DeBoo, J.C., *et al*. 2012 *Phys. Plasmas* **19** 082518

[38] Hillesheim, J.C., *et al. EPS, Proc. of the 39th Conf. on Plasma Physics, (Stockholm, SE, 2012)*, submitted to Phys. Rev. Lett. (2012).

[39] Rhodes, T.L., personal communication, September 2012

[40] Solomon, W.M., Burrell, K.H., deGrassie, J.S., Boedo, J.A., Garofalo, A.M., Moyer, R.A., Muller, S.H., Petty, C.C., and Reimerdes, H., 2011 *Nucl. Fusion* **51** 073010

[41] Grierson, B.A., Burrell, K.H., and Solomon, W.M., *IAEA, Proc. of the 24th IAEA Fusion Energy Conf. (San Diego, CA, 2012)* Paper EX/P3-9

[42] Grierson, B.A., Burrell, K.H., Heidbrink, W.W., Lanctot, M.J., Pablant, N.A., and Solomon, W.M., 2012 *Phys. Plasmas* **19** 056107

[43] Tobias, B.J., Classen, I.G.J., Domier, C.W., Heidbrink, W.W., Luhmann, Jr., N.C., Nazikian, R., Park, H.K., Spong, D.A., and Van Zeeland, M.A., 2011 *Phys. Rev Lett*. **106** 075003

[44] Heidbrink, W.W., *et al*., *IAEA, Proc. of the 24th IAEA Fusion Energy Conf. (San Diego, CA, 2012)* Paper EX/P6-22

[45] Hanson, J.M., *et al*., *IAEA, Proc. of the 24th IAEA Fusion Energy Conf. (San Diego, CA, 2012)* Paper EX/P4-27

[46] Kramer, G.J., *et al*., *IAEA, Proc. of the 24th IAEA Fusion Energy Conf. (San Diego, CA, 2012)* Paper ITR/P1-32

[47] Doyle, E.J., *et al*. 2007 *Nucl. Fusion* **47** S18

[48] Schmitz, L. 2012 *Phys. Rev. Lett.* **108** 155002

[49] Schmitz, L., *et al.*, *IAEA, Proc. of the 24th IAEA Fusion Energy Conf. (San Diego, CA, 2012)* Paper EX/P7-17

[50] Tynan, G., *et al.*, *IAEA, Proc. of the 24th IAEA Fusion Energy Conf. (San Diego, CA, 2012)* Paper EX/10-3

[51] Yan, Z., *et al.*, *IAEA, Proc. of the 24th IAEA Fusion Energy Conf. (San Diego, CA, 2012)* Paper EX/P7-05

[52] Gohil, P., *et al.*, *IAEA, Proc. of the 24th IAEA Fusion Energy Conf. (San Diego, CA, 2012)* Paper ITR/P1-36

[53] Luce, T.C. 201 *Phys. Plasmas* **18** 030501

[54] Murphy, C.J., *et al. IEEE/NPSS 24th Symp. on Fusion Engineering (SOFE) (Chicago, IL, 2011)*

[55] Van Zeeland, M.A., *et al.*, *EPS, Proc. 39th EPS Conf. Plasma Physics (Stockholm, Sweden, 2012)* http://ocs.ciemat.es/epsicpp2012pap/html/author.html, Paper P2.068

[56] Park, J.M., *et al.*, *IAEA, Proc. of the 24th IAEA Fusion Energy Conf. (San Diego, CA, 2012)* Paper EX/P2-13

[57] Holcomb, C.T., *et al.*, *IAEA, Proc. of the 24th IAEA Fusion Energy Conf. (San Diego, CA, 2012)* Paper EX/1-5

[58] Garofalo, A.M., *et al.*, *IAEA, Proc. of the 24th IAEA Fusion Energy Conf. (San Diego, CA, 2012)* Paper FTP/P7-35

[59] Ryutov, D. 2007 *Phys. Plasmas* **14** 064502

[60] Allen, S.L., *et al.*, "Initial Snowflake Divertor Physics Studies on DIII-D," *IAEA, Proc. of the 24th IAEA Fusion Energy Conf. (San Diego, CA, 2012)* Post-deadline

submission

[61] Makowski, M.A., *et al*., 2012 *Phys. Plasmas* **19** 056122

[62] Makowski, M.A., *et al*., *IAEA, Proc. of the 24th IAEA Fusion Energy Conf. (San Diego, CA, 2012)* Paper EX/P5-16

[63] Eich, T., *et al*., *IAEA, Proc. of the 24th IAEA Fusion Energy Conf. (San Diego, CA, 2012)* Paper ITR/1-1

[64] Rudakov, D.L., *et al*., *IAEA, Proc. of the 24th IAEA Fusion Energy Conf. (San Diego, CA, 2012)* Paper EX/P5-11

List of Figure Captions

Fig. 1. (Color online) Example discharge showing $n = 3$ RMP ELM suppression in DIII-D at ITER I/aB and low ν^* with ITER-like shape (#150458). (a) Divertor H_α and RMP coil current showing complete suppression after 3.5 s. (b) Similarity to key discharge parameters in ITER. (c) Neutral beam and EC heating power.

Fig. 2. (Color online) DIII-D plasma shape for RMP ELM suppression experiments (dashed), compared to scaled ITER scenario 1 shape. Outer divertor strike point positioned to provide density control by divertor pumping.

Fig. 3. (Color) ELM pacing with 1.3 mm deuterium; no pellets (black) vs 60 Hz pellets (red). (a) Outer SOL H_α brightness shows variation in pellet timing due to variations in guide tube transit time. (b) Transient divertor heat pulse $[\iint 2\pi R_q(r)drdt]$. (c) Line-average density.

Fig. 4. (Color online) Peak divertor heat flux vs pellet rate, showing $1/f$ dependence. Without pellets, ELMs naturally occur at 5 Hz rate.

Fig. 5. (Color) H-mode pedestal evolution between ELMs. (a) Plasma pressure profiles derived from Thomson scattering and charge exchange recombination data vs normalized flux (separatrix at $\psi_N = 1.0$) from (1) right after an ELM (1) to (8) just before the next ELM; markers indicate location of peak pedestal pressure. (b) Peak pedestal pressure evolution compared to EPED model.

Fig. 6. (Color) Tangential soft x-ray X-point difference imaging data showing filamentary structure near the X-point arising from $n = 3$ RMP, as compared to simulation. Color intensity indicates magnitude of change in SXR brightness as RMP phase changes by $\pi/3$. Red/blue indicate phase of intensity change ($\pm$) relative to perturbation change. Synthetic diagnostic data from simulation uses model calculated temperature perturbation and assumes uniform carbon concentration.

Fig. 7. (Color online) (a) Images of synchrotron emission from disruption-induced runaway electrons with overlay of limiting current-channel flux surface inferred with EFIT. 140 ms elapsed time when hot core contacts inner wall. (b) Plasma current showing enhanced RE dissipation with argon injection before thermal quench. (c) Plasma current traces with neon and helium MGI after thermal quench, showing increased RE dissipation with higher-Z gas.

Fig. 8. (Color online) Low-torque ITER simulation discharge (Scenario 1) with low rotation. (a) β_N and ℓ_i, (b) torque showing range of ITER-equivalent torques and ECCD power, (c) density and ECCD power, (d) H-mode energy confinement factor (H_{98y2}).

Fig. 9. (Color online) ELM-free QH-mode (solid circles) and ELMing H-mode (solid diamonds) confinement factor vs edge (r/a=0.8) toroidal rotation velocity.

Fig. 10. (Color) Neoclassical tearing mode control showing time traces of (a) launcher mirror position tracking requested position, (b) location of $q = 2$ surface superimposed

on colorized ECCD intensity plot as derived from ONETWO profile analysis and EC ray tracing, (c) ECCD power and 2/1 tearing mode amplitude from edge magnetic probes.

Fig. 11. (Color online) Error field correction experiments using (a) external C-coil to produce $n = 1$ error field and internal I-coils to provide correction. (b) Neoclassical rotational damping torque for the proxy error field, correction coils and combined proxy error and correction coils.

Fig. 12. (Color online) L-mode critical-gradient electron stiffness in DIII-D. (a) Change in ECH location an resulting change in electron temperature profile. (b) Resulting change in electron heat flux at $\rho = 0.6$. (c) Resulting electron temperature fluctuations at $\rho = 0.5$. TGLF simulation (triangle), GYRO simulation (square) results.

Fig. 13. (Color) Measured H-mode ion and electron temperature profiles vs TGLF simulation predictions using measured T_e and T_i at r=0.85 as boundary condition. 3 MW NBI heating (black); 7 MW NBI heating (red). TGLF simulations (solid line with square).

Fig. 14. (Color online) Predicted vs measured intrinsic torque for H-mode plasmas, with prediction for ITER using same methodology as in reference 15.

Fig. 15. (Color) Measured pedestal height vs predicted pedestal height from the EPED model for 270 tokamak discharges from five tokamaks as shown. Predicted pedestal height for ITER (diamond symbol at upper right) agrees with design target value for $Q = 10$ operation.

Fig. 16. (Color) Limit cycle oscillations during a "dithering" H-mode transition. (a) Divertor H_α brightness showing oscillations starting from L-mode at 1272 ms and ending with steady H-mode at 1289 ms. (b) microwave Doppler backscattering data for $k_\theta \rho_s \sim 0.5$ measured between 1–2 cm inside the separatrix. Red and green indicate H-mode and L-mode data, respectively. Blue and green data from two neighbouring channels during the limit cycle.

Fig. 17. (Color online) Off-axis NBI on DIII-D. (a) NUBEAM calculation showing starting location for fast ions created from beam-injected neutrals for on-axis and full 16.5 off-axis injection. Path curvature results from projection of tangential beam path onto cross section. (b) Neutral beam current drive from Ohm's law and time evolution of magnetic flux with error bars as indicated. Solid lines show NUBEAM predictions.

Fig. 18. (Color online) Stationary high β_N, high q_{min} discharges maintained with off-axis NBI and ECCD.

Fig. 19. (Color online) Current and pressure profiles for steady-state discharges with off-axis NBI compared to previous results with on-axis NBI only.

Fig. 20. (Color) Ideal-wall $n = 1$ β_N limits calculated by DCON for Advanced Tokamak discharges with both off-axis (+ filled boxes) and on-axis NBI (+ only) as function of pressure peaking and internal inductance. Red symbols have β_N limit >4 and blue have β_N limit <4.

Fig. 21. (Color online) Stationary high β_N H-mode discharges with q_{min} ~ 1.5 maintained for $2\tau_R$ with off-axis NBI and ECCD. Typical discharge with on-axis NBI

(118419); recent discharge with off-axis NBI (147634). Minimum safety factor generally near $\rho \sim 0.4 - 0.5$. Without sufficient off-axis current drive, $n = 1$ tearing mode grows and ends discharge 118419.

Fig. 22. (Color online) Conventional (left) vs Snowflake-minus (reference 56) divertor configuration (right) in DIII-D.

Fig. 23. (Color) Compared to standard divertor (black), Snowflake-minus (red) increases divertor flux expansion, $B_{\mathrm{pol,mid}}/B_{\mathrm{pol,div}}$, in (a); reduces peak inter-ELM heat flux (b); and reduces energy loss per ELM in (c).

Fig. 24. (Color) D_2 gas puffing in Snowflake-minus significantly increases radiative power loss in the divertor (top) and reduces surface heat flux to very low values (bottom), including ELM pulses. Rectangular 2D image of divertor heat flux radial profiles vs time as measured by IR TV (red corresponds to higher heat flux than blue).

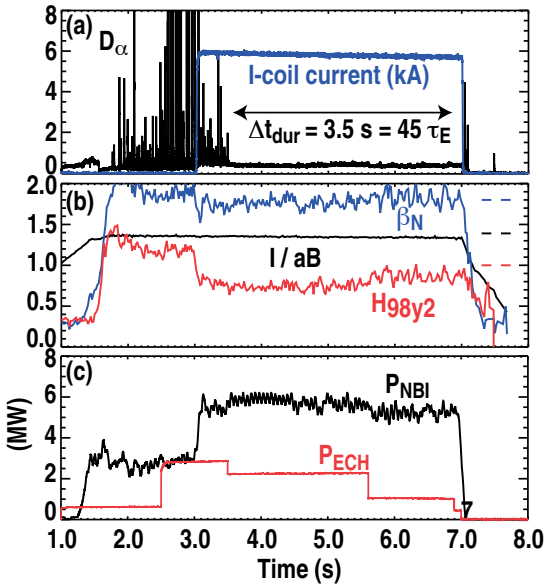

D.N. Hill Figure 1

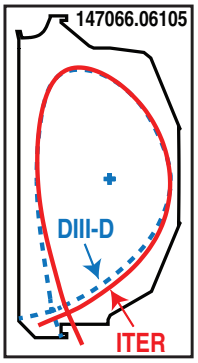

D.N. Hill Figure 2

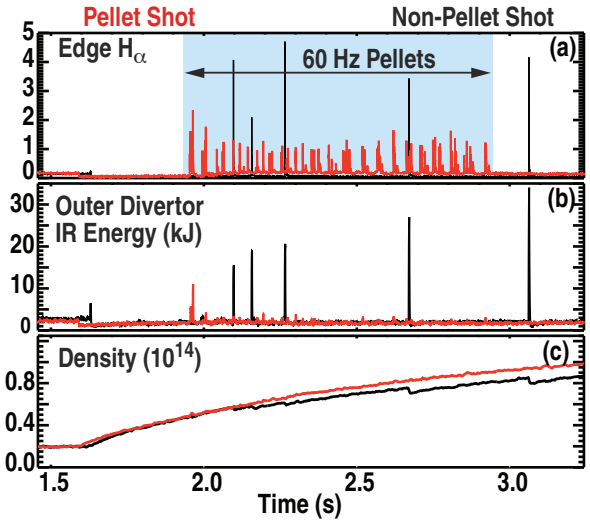

D.N. Hill Figure 3

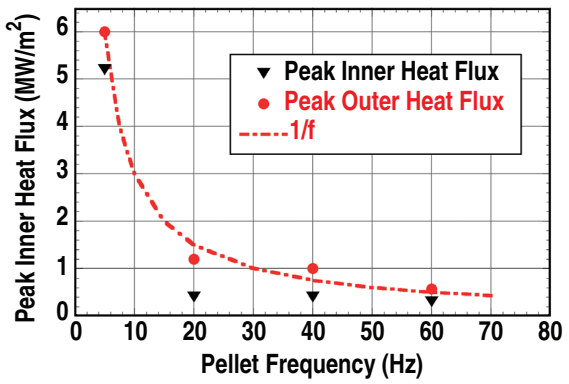

D.N. Hill Figure 4

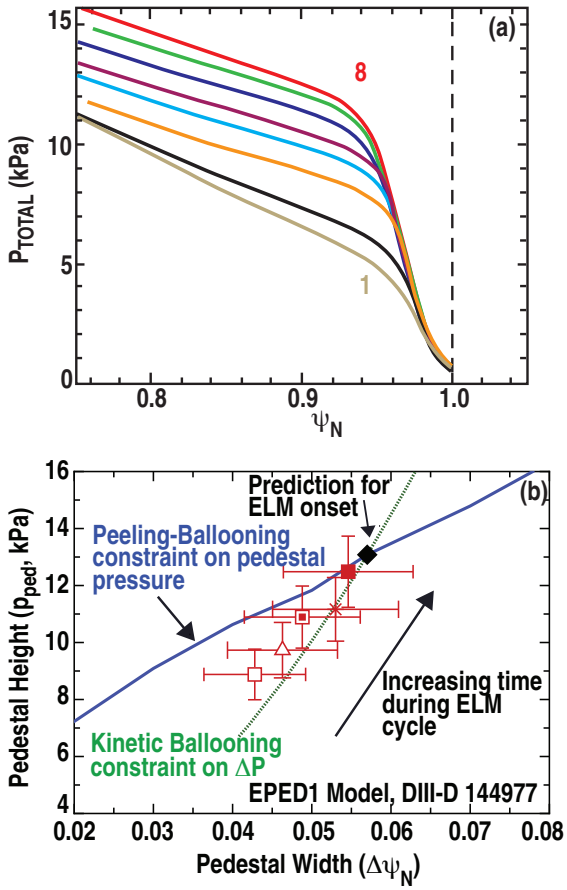

D.N. Hill Figure 5

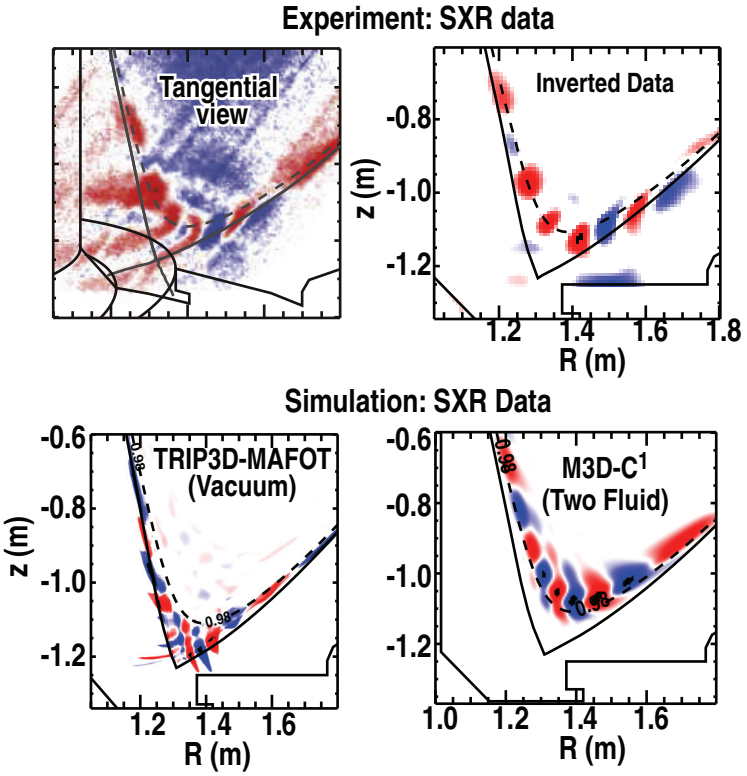

D.N. Hill Figure 6

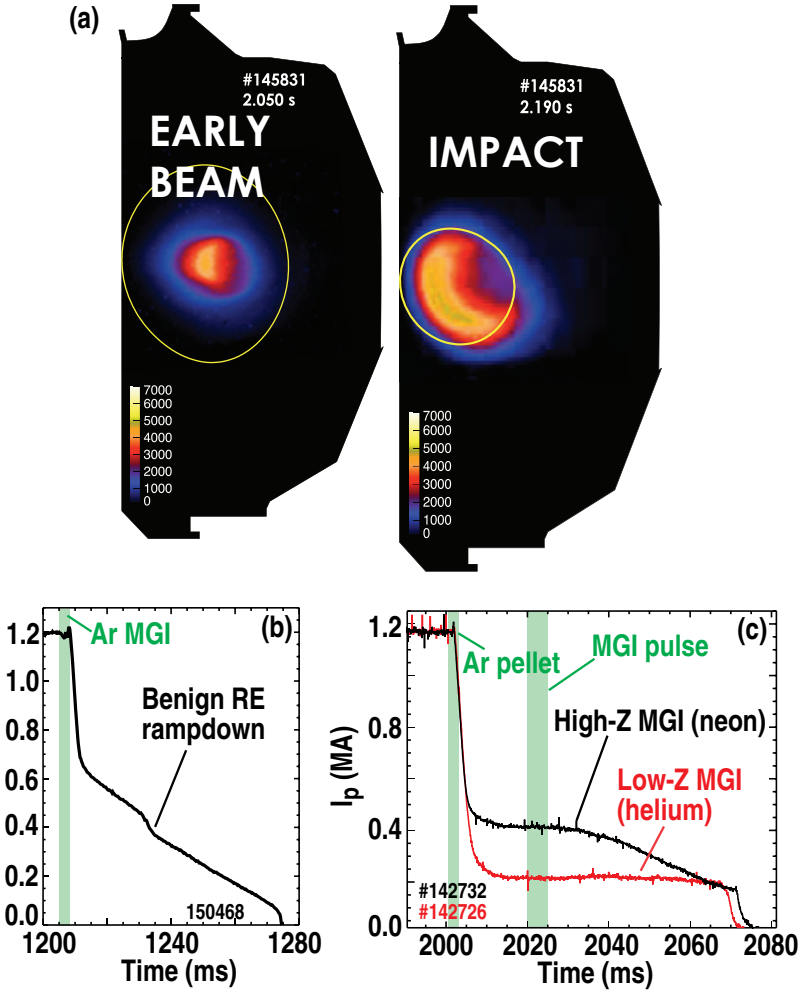

D.N. Hill Figure 7

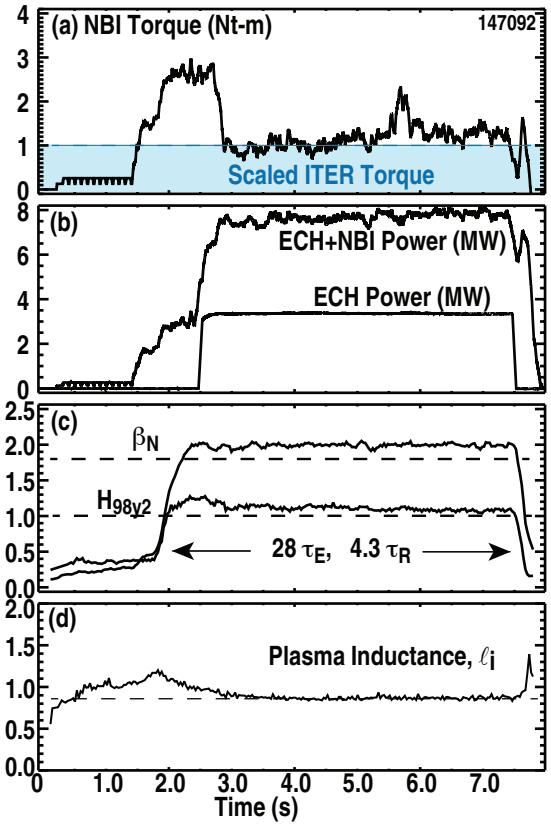

D.N. Hill Figure 8

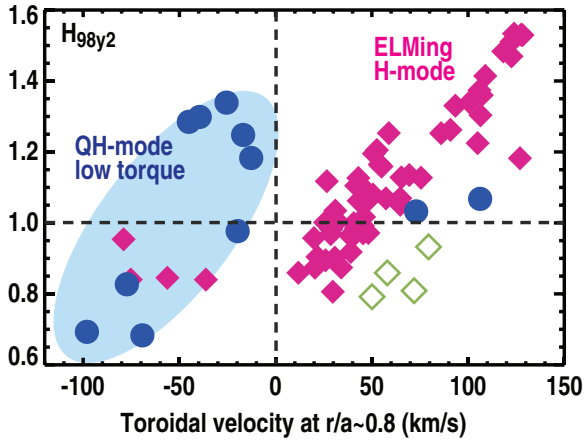

D.N. Hill Figure 9

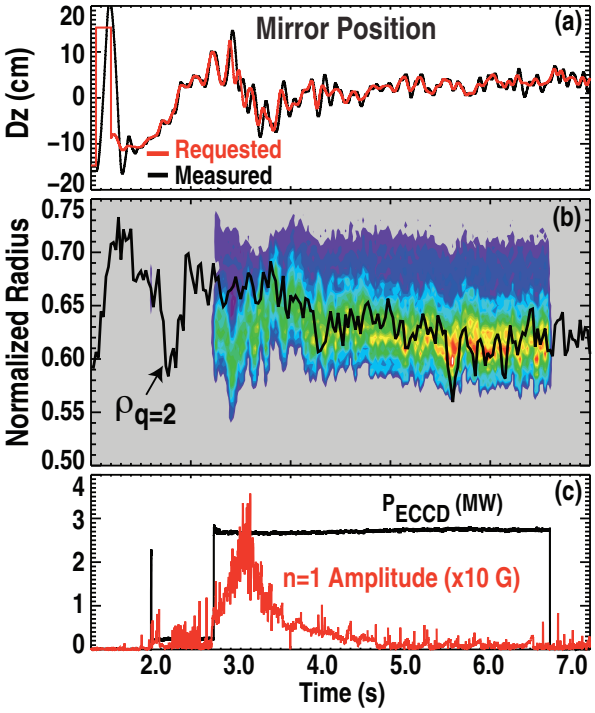

D.N. Hill Figure 10

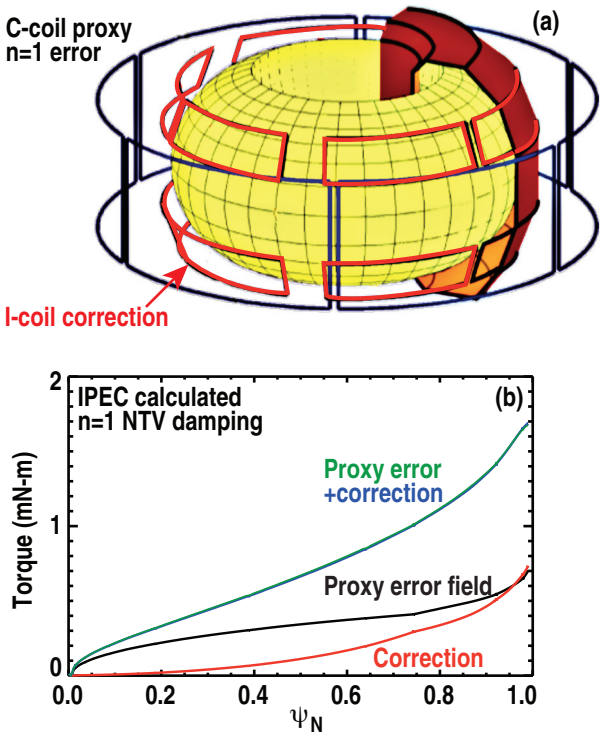

D.N. Hill Figure 11

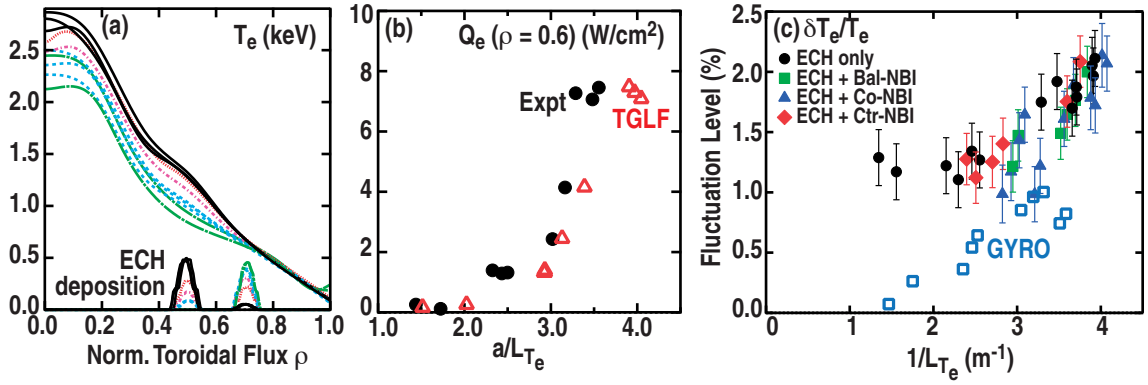

D.N. Hill Figure 12

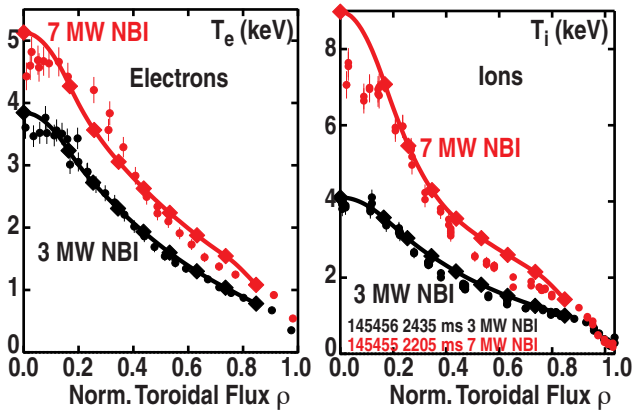

D.N. Hill Figure 13

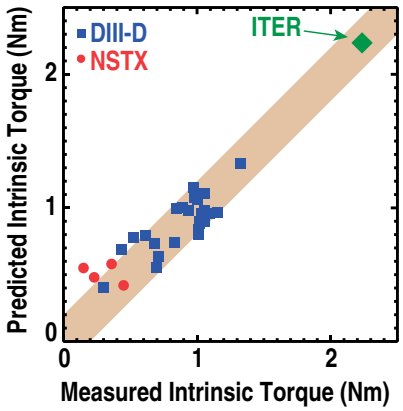

D.N. Hill Figure 14

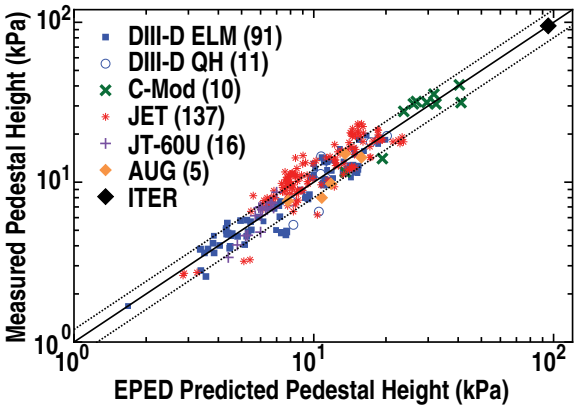

D.N. Hill Figure 15

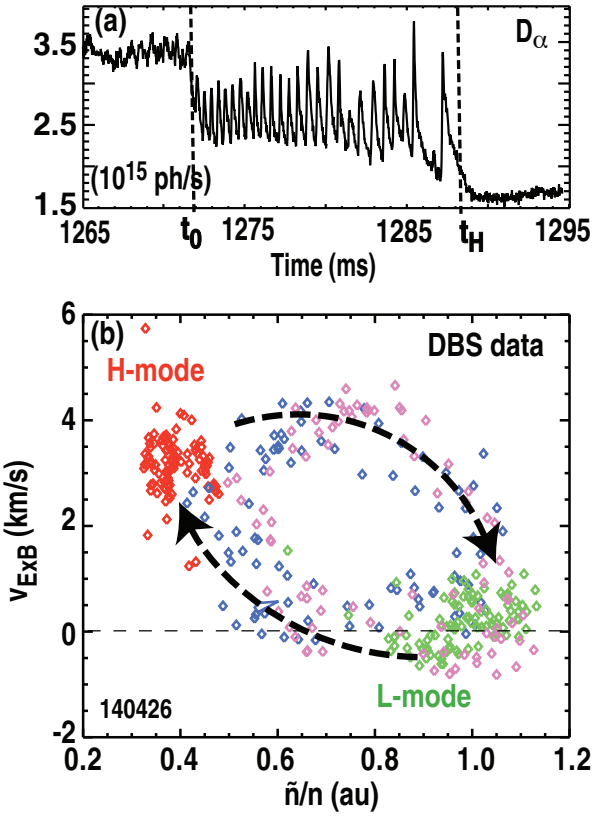

D.N. Hill Figure 16

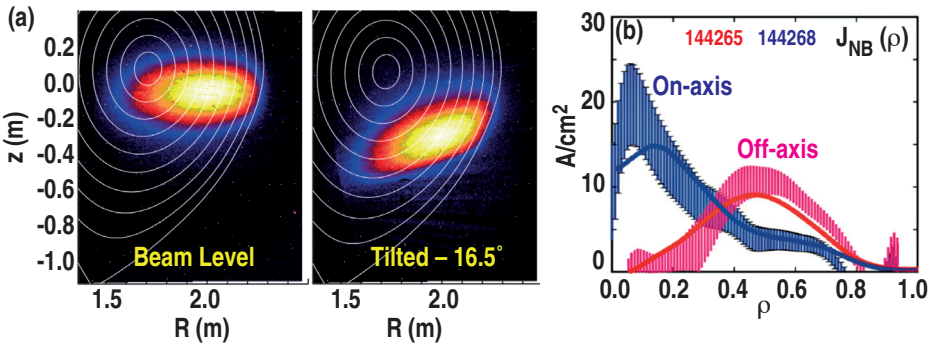

D.N. Hill Figure 17

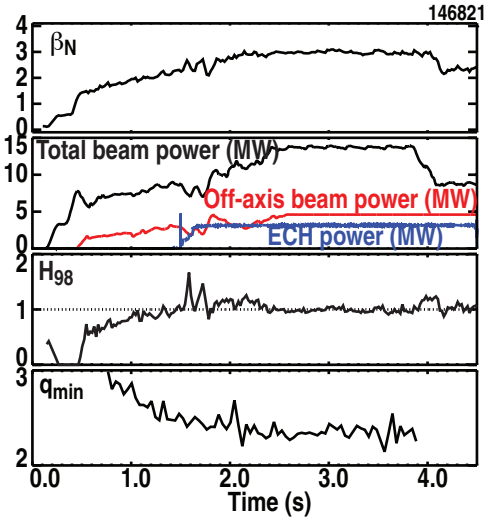

D.N. Hill Figure 18

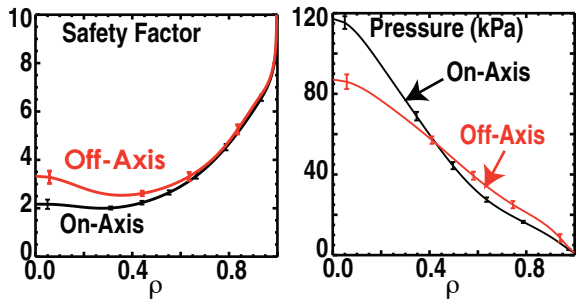

D.N. Hill Figure 19

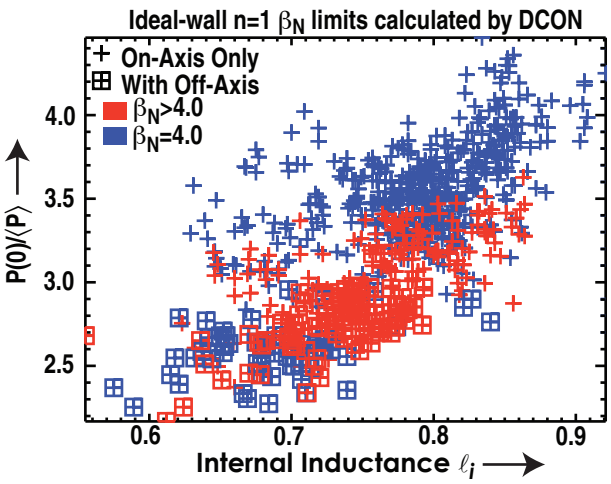

D.N. Hill Figure 20

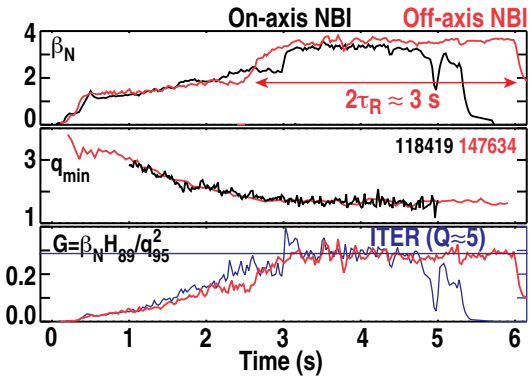

D.N. Hill Figure 21

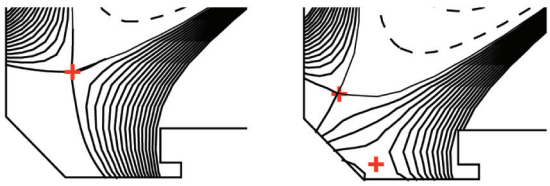

D.N. Hill Figure 22

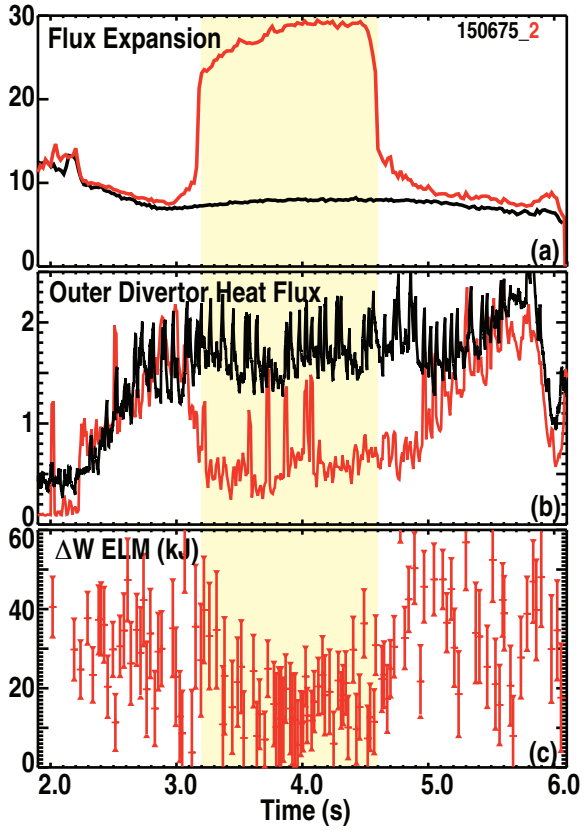

D.N. Hill Figure 23

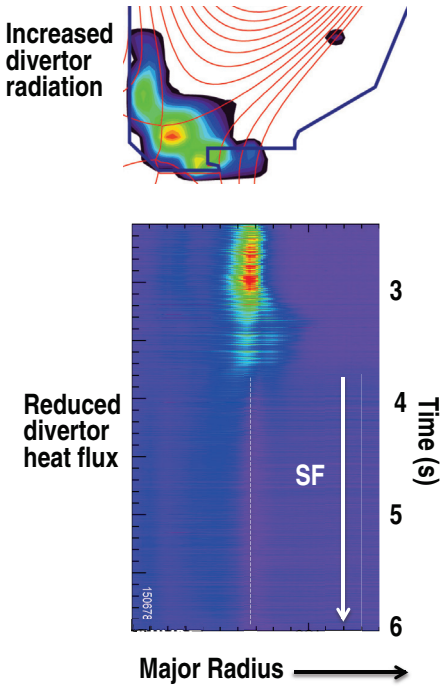

D.N. Hill Figure 24